

LETTER TO THE EDITOR

# Equilibrium figure of Haumea and possible detection by stellar occultation

C. Staelen<sup>1</sup>, N. Rambaux<sup>2</sup>, F. Chambat<sup>3</sup>, and J. C. Castillo-Rogez<sup>4</sup>

<sup>1</sup> Université Paris Cité, CNRS, Institut de Physique du Globe de Paris, F-75005 Paris, France  
e-mail: staelen@ipgp.fr

<sup>2</sup> Sorbonne Université, Observatoire de Paris, Université PSL, CNRS, Laboratoire Temps Espace, F-75014 Paris, France

<sup>3</sup> Université de Lyon, CNRS, ENS Lyon, Laboratoire de Géologie de Lyon Terre - Planètes - Environnement, F-69007 Lyon, France

<sup>4</sup> Jet Propulsion Laboratory, California Institute of Technology, Pasadena, California, USA

Received ??? / Accepted ???

## ABSTRACT

The equilibrium figure of dwarf planet Haumea is studied to determine if the observed shape is compatible with a differentiated hydrostatic body. Three groups of interior models of Haumea are assumed, all with a rocky core and a volatile-rich outer shell that may contain some porosity. A third layer located between the core and the outer shell has a density suggesting partial differentiation or the presence of a large fraction of organic matter. Using the code BALEINES, which solves for the equilibrium figures of the boundaries between layers, we show that the hydrostatic models closest to the shape derived by stellar occultation approach a state of critical rotation, which translates into a pinched shape with large deviations from an ellipsoid (up to 110 km). The previous stellar occultation and light curves cannot distinguish between the ellipsoid and the pinched shape, but we predict this figure could be observable on the next stellar occultation of Haumea on May 4, 2026, if some chords are obtained in the northern or southern limbs of the shadow.

**Key words.** Kuiper belt objects: individual: (136108) Haumea, planets and satellites: interiors, gravitation, methods: numerical

## 1. Introduction

(136108) Haumea is a rapidly rotating Kuiper belt object whose triaxial figure was estimated by [Ortiz et al. \(2017\)](#) from a stellar occultation together with light curves. The resulting best-fit ellipsoid has semi-axes lengths  $a = 1161 \pm 30$  km,  $b = 852 \pm 4$  km and  $c = 513 \pm 16$  km. As noted by these authors, this geometry is incompatible with a Jacobi ellipsoid, i.e. a homogeneous ellipsoid in hydrostatic equilibrium. This discrepancy implies that either rigid-body forces provide significant support against self-gravity, or Haumea has undergone differentiation and is thus heterogeneous. The former possibility questions Haumea's classification as a dwarf planet, as hydrostatic equilibrium is a requirement. Therefore, a detailed examination of its equilibrium figure may help refining the distinction between hydrostatic and non-hydrostatic bodies (see also [Chambat et al. 2023](#); [Vermersch et al. 2025](#)).

[Dunham et al. \(2019\)](#) and [Noviello et al. \(2022\)](#) have studied two layer hydrostatic models of Haumea, with a rocky core and an icy mantle. Although differentiation allows these models to get closer to Haumea's observed shape, no configuration can fully reproduce it. [Kondratyev \(2016, 2024\)](#) analytically treated the interior as a pair of confocal ellipsoids, but [Hamy \(1889\)](#) demonstrated that rigidly rotating ellipsoidal stratifications cannot satisfy hydrostatic equilibrium. Thus, the question of Haumea's hydrostaticity is still open. Furthermore, a new stellar occultation by Haumea is predicted for May 4 2026<sup>1</sup>, which may refine the observational constraints on its shape.

In this letter, we investigate the range of triaxial equilibrium figures of two- and three-layer hydrostatic bodies. Unlike previous works, we show that, if Haumea has a hydrostatic shape, then it may deviate significantly from an ellipsoid and could even be pinched at the end of its equatorial major axis, indicating a state of critical rotation. Finally, we question whether observational data from May 2026 can discriminate an ellipsoid from a pinched figure.

## 2. Methods

The theory of equilibrium figures states that a rigidly rotating fluid mass is in hydrostatic equilibrium if and only if the surfaces of constant density and the surfaces of constant effective potential, i.e. the sum of the centrifugal and self-gravitational potentials, coincide (e.g. [Zharkov & Trubitsyn 1978](#); [Lanzano 1982](#)). Determining an equilibrium figure then comes down to finding shapes of the fluid whose effective potential is constant on these surfaces. As the potential depends non-trivially on the shape, the corresponding equations set actually forms a fixed-point problem. In this paper, we consider a differentiated body composed of  $L = 2$  or  $3$  homogeneous layers, indexed by  $\ell$  with  $\ell = 1$  denoting the innermost layer and  $\ell = L$  the outermost. Assuming homogenous layers is sufficient since under the low pressures inside Haumea ( $\lesssim 500$  MPa), the densities of ices and rocky minerals increase only by a few percent (the bulk moduli are  $\sim 10$  GPa for ices and  $\gtrsim 100$  GPa for rocks). We use the code BALEINES ([Staelen & Huré 2026](#)), which computes iteratively the shapes of the interfaces. Each surface is expanded over Chebyshev polynomials both for latitude and longitude, the

<sup>1</sup> <https://lesia.obspm.fr/lucky-star/occ.php?p=156331>

potential is written in term of surface integrals only, and these integrals are computed with Clenshaw-Curtis quadratures. Mirror symmetry with respect to the plane ( $xOy$ ) is imposed by the Lichtenstein theorem, and mirror symmetry with respect to the planes ( $yOz$ ) and ( $zOx$ ) is assumed to reduce the computation times,  $O$  being the centre of mass, ( $Ox$ ), ( $Oy$ ) and ( $Oz$ ) coinciding with its equatorial major, equatorial minor and polar axes, respectively. Here, 17 Chebyshev nodes are used both for latitude and longitude, which results in a relative precision of the order of  $10^{-4}$ .

Let  $a_\ell$ ,  $b_\ell$  and  $c_\ell$  be the equatorial major semi-axis, the equatorial minor semi-axis and the polar axis of the boundary of layer  $\ell$  and  $\rho_\ell$  its mass density. The explored parameters of the models reported in this work are  $c_L/a_L$ ,  $\rho_\ell/\rho_{\ell+1}$  ( $1 \leq \ell < L$ ) and  $c_\ell/c_L$ . All quantities in BALEINES are normalised by the length of the equatorial major semi-axis and the mass density of the outermost layer of the fluid mass,  $a_L$  and  $\rho_L$ . The physical outputs are then obtained by requiring that the mass and the length of the minor equatorial semi-axis match the values currently determined for Haumea, i.e.  $M = (3.952 \pm 0.011) \times 10^{21}$  kg (Proudfoot et al. 2024) and  $b_L = 852 \pm 4$  km (Ortiz et al. 2017). We make the choice to impose  $b_L$  since it is the best constrained semi-axis length. This is because the major equatorial axis of Haumea was nearly pointing towards the Earth during the 2017 occultation, meaning that the semi-major axis of the projected ellipse corresponds to the value of  $b_L$ .

### 3. Hydrostatic shape models and compatibility with the 2017 occultation

Starting from two- and three-layer models of Haumea, we explore a large range of the parameter space:  $\rho_\ell/\rho_{\ell+1} \in [1.2, 4.2]$ ,  $c_1/c_2 \in [0.25, 0.95]$  for two layers,  $c_2/c_3 \in [0.30, 0.95]$  and  $c_1/c_3 \in [0.25, c_2/c_3]$  for three layers, and  $c_L/a_L \in [0.42, 0.52]$ . The results are summarised in figure 1, which displays, in the  $(c_L/a_L, b_L/a_L)$ -plane, the region where hydrostatic models have been found. As expected, heterogeneity expands the possible ranges of  $b_L/a_L$  for a given  $c_L/a_L$ , while only a unique value is permitted in the homogeneous case. The hydrostatic figures are contained between two curves into the  $(c_L/a_L, b_L/a_L)$ -plane: the curve at higher  $c_L/a_L$  is given by models with a large outer layer (Staelen & Huré 2026), while the curve at lower  $c_L/a_L$  corresponds to configurations at the mass-shedding limit, that is to say the centrifugal acceleration,  $\Omega^2 a_L$ ,  $\Omega$  being the rotation rate, exactly balances the self-gravity at the end of the equatorial major axis,  $g_a$ . To measure the proximity to this limit, we define  $q = \Omega^2 a_L / |g_a|$ , so that the mass-shedding limit, or critical rotation, is defined by  $q = 1$ .

From the explored space, we select six configurations, labelled from A to F, whose free surface shapes are coherent with the chords obtained during the 2017 occultation event. Figure 2 shows that their boundaries are quite elliptical in the ( $yOz$ ) plane but significantly deviate from an ellipse in the ( $xOz$ ) plane, up to pinched shape for configurations B, C and E. The maximal deviations from an ellipsoid are approximately of 60 km for configurations A and D and 110 km for the pinched configurations. The properties of these six configurations are reported in table 1. We also project their free surface onto the sky plane at the epoch of the 2017 occultation; see figure 3. To do so, we use the Chebyshev expansion to resample the shape of the free surface, and form a regular triangular mesh with 15155 facets that we use as an input file for the open-access tool developed by Rizos et al. (2025). These projections confirm that hydrostatic models are able to fit the occultation chords. Light curves obtained

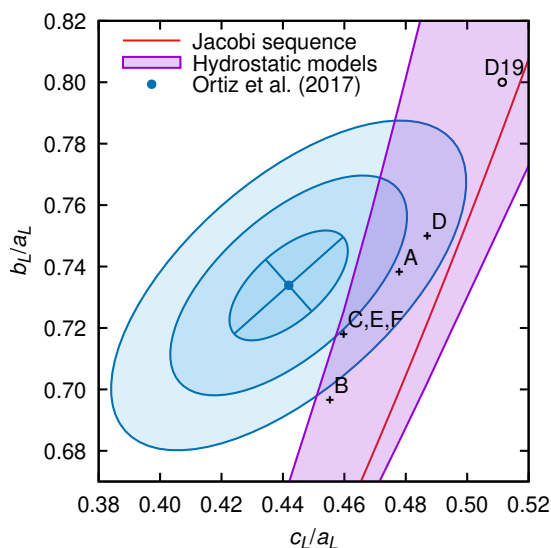


**Fig. 1.** Possible hydrostatic models obtained in this work (pink region) compared with the Jacobi sequence (red line). The models of table 1 are plotted with black crosses; “D19” corresponds to the hydrostatic model preferred by Dunham et al. (2019). The best-fit ellipsoid obtained by Ortiz et al. (2017) is reported as well and plotted with  $1, 2$  or  $3\sigma$  uncertainty regions.

with these shapes are reported in Appendix A and show that hydrostatic models are also able to fit the light curves obtained by Lacerda et al. (2008), Lockwood et al. (2014) and Ortiz et al. (2017). Finally, the values of  $J_2$  obtained in this work are compatible with the corresponding observation: they range between 0.144 and 0.157, which lies at the bottom of the  $1\sigma$  confidence region obtained by Proudfoot et al. (2024) by orbit fitting, i.e.  $J_2^{\text{obs}} = 0.262^{+0.103}_{-0.112}$ .

Notice, that in figure 1, our closest hydrostatic models to the best-fit ellipsoid of Ortiz et al. (2017) (models C and E) have figures that deviate greatly from an ellipsoid. However, this deviation is actually very small in the plane ( $yOz$ ) containing the polar and the equatorial minor axes, see figure 2, which corresponds roughly to the plane that was observed by stellar occultation in 2017. As a consequence, shapes that greatly deviate from an elliptical shape in the plane ( $xOz$ ) can match the 2017 occultation data as well as an ellipsoid.

## 4. Discussion

### 4.1. Haumea as a critical rotator

Some hydrostatic figures exhibit a pinched geometry, i.e. the surface normal becomes discontinuous at the end of the major equatorial axis. Since the effective gravity is continuous and, for a hydrostatic body, orthogonal to the equipotential surfaces, this behaviour is possible only if the effective gravity vanishes at that point, i.e. for critical rotators ( $q = 1$ ). This is illustrated by configurations B, C and E, whose values of  $q$ , reported in table 1 are between 0.96 and 0.99. It is noteworthy that pinched shapes for critical rotators are actually well documented in the context of stellar physics (e.g. Maeder & Meynet 2012). Furthermore, such equatorial ridges have been observed at several fast-rotating asteroids as (2867) Šteins (Jorda et al. 2012) and (65803) Didymos (Barnouin et al. 2024). Also, note that even configurations A and D are close to the mass-shedding limit ( $q \in [0.75 - 0.80]$ , which corresponds to 85 – 90 % of the critical rotation rate).

**Table 1.** Examples of hydrostatic solutions whose free surface is coherent with the chords obtained during the 2017 occultation (Ortiz et al. 2017).

	$L$	$\frac{c_L}{a_L}$	$\frac{\rho_1}{\rho_2}$	$\frac{\rho_2}{\rho_3}$	$\frac{c_1}{c_L}$	$\frac{c_2}{c_L}$	$q$	$a_L$ (km)	$c_L$ (km)	$R$ (km)	$\rho_3$ (kg/m <sup>3</sup> )	$\rho_2$ (kg/m <sup>3</sup> )	$\rho_1$ (kg/m <sup>3</sup> )	$\tau$ (hr)	$J_2$
A	3	0.478	1.8	1.8	0.80	0.85	0.80	1154	551	792	903	1626	2927	3.91	0.157
B	3	0.455	1.8	2.2	0.65	0.90	0.96	1223	557	795	856	1889	3400	3.92	0.156
C	3	0.460	2.6	1.4	0.78	0.90	0.99	1187	546	780	927	1315	3420	3.72	0.144
D	3	0.487	1.8	2.6	0.40	0.85	0.75	1136	553	790	970	2523	4542	3.91	0.157
E	3	0.460	1.4	3.4	0.25	0.81	0.98	1190	547	782	932	3212	4496	3.76	0.145
F	2	0.460	3.8	–	0.82	–	0.98	1182	544	781	–	830	3196	3.75	0.145

**Notes.** In all configurations,  $M = (3.952 \pm 0.011) \times 10^{21}$  kg and  $b_L = 852 \pm 4$  km. The reference radius for  $J_2$  is 798 km as that of Proudfoot et al. (2024). The relative uncertainties obtained by propagating that of  $M$  and  $b_L$  are 1.7 % for the mass densities, 0.5 % for the lengths and 0.8 % for the rotation periods; it implies that this source of uncertainty is negligible with respect to the variability of the models and that some rotation periods we obtain are statistically not different from the observed one.

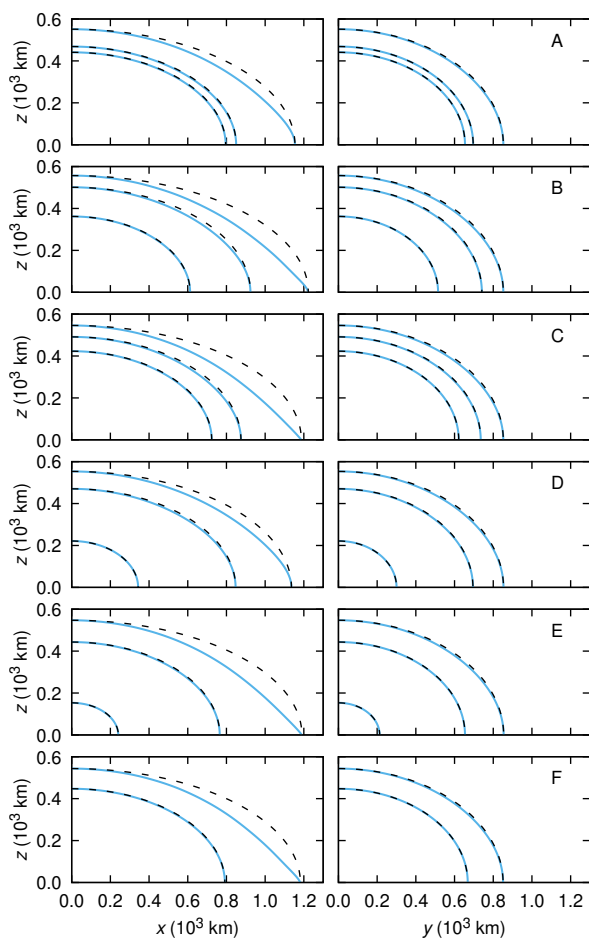


**Fig. 2.** Hydrostatic shape models for Haumea in the  $(xOz)$  (left) and  $(yOz)$  (right) planes, corresponding to the configurations reported in table 1. The dashed lines correspond to the ellipsoids with the same axis lengths as the layers' boundary.

#### 4.2. Haumea's shape as a fossil figure

As shown by configurations A, B and D, some models are fully compatible with the 2017 occultation and the observed rotation period of Haumea. However, Haumea's shape could also be "frozen", i.e. representative from a previous rotation state, and would then depart from hydrostatic equilibrium; this is why we have not imposed our models to exactly fit the observed rotation period. The rotation periods of configurations C, E and F are 9.3 to 11.6 minutes shorter than the observed value, imply-

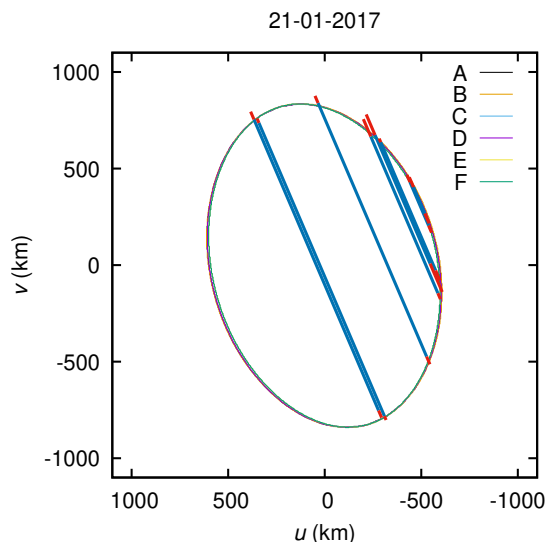


**Fig. 3.** Projections of the six hydrostatic representative solutions in the sky plane at the epoch of the 2017 occultation.  $u$  and  $v$  are the celestial East and North, respectively.

ing a relative difference of roughly 5 %. In the formation scenario hypothesized by Noviello et al. (2022), Haumea's rotation was slowed through hydration of the rocky core by hydrothermal circulation that generated a redistribution of mass and increased its moment of inertia. Tidal migration of satellites represents another mechanism capable of decreasing a planet's spin rate. From the conservation of angular momentum in the whole system, and assuming circular orbit in the equatorial plane of Haumea for the satellites, one can derive the coupled evolution of the primary's rotation and the satellites' orbits (Murray & Dermott 1999). However, considering the low masses and the orbital parameters of Hi'iaka and Namaka obtained by Proudfoot et al. (2024) and  $k_2/Q \lesssim 10^{-2}$ , the computed timescales are longer than the age of the Solar system. Thus, tidal migration alone cannot account for Haumea's present spin state. Additional spin-down could have occurred through small impacts, potentially involving debris from its ring. However, as demonstrated by configuration B, critical rotators can also be consistent with the observed rotation period, implying that a spin-down is not mandatory for Haumea to have a pinched shape.

### 4.3. Internal structures

The mean densities of our hydrostatic models range from 1899 to 2058 kg/m<sup>3</sup>, which lies between Pluto's (1853±4 kg/m<sup>3</sup>, Brozović & Jacobson 2024) and Eris' (2430±50 kg/m<sup>3</sup>, Holler et al. 2021), and is consistent with the densities expected for material condensed in the Kuiper belt (Barr & Schwamb 2016).

Composition-wise, three groups of models have been identified from our exploration of the parameter space. All three of them can be summed up as a rocky core and a thick volatile-rich shell, coherent with the structures reported by Dunham et al. (2019) and Noviello et al. (2022). The first one consists in a two-layer structure with a “low” mass density shell, up to 830 kg/m<sup>3</sup> thick overlaying a rocky core, like configuration F in table 1. The low shell density may be interpreted as 12-17% of porosity (averaged), assuming a pure ice composition, or about 55% porosity assuming an undifferentiated water-rock-organic-rich shell and taking as a reference the aforementioned mean density of 1900 kg/m<sup>3</sup>. The second group consists in three-layer configurations, among which configurations A, B and C, with an outer volatile-rich shell, a rocky core, and a thin mantle in between. The latter has a density between 1200 and 1500 kg/m<sup>3</sup>. This may indicate partial separation of the rock from the volatile phase or the presence of a high fraction of insoluble organic matter (McKinnon et al. 2020). In this line of models, the shell could have a density as high as 980 kg/m<sup>3</sup>, corresponding to a non-porous, pure ice region. The last group of models also consists in three-layer structures, including configurations D and E, similar to the two-layer models but with the addition of a small inner core with a density ≥ 4500 kg/m<sup>3</sup>, which suggests the concentration of metal-rich phases (e.g., magnetite) mixed with silicates.

From a thermal evolution standpoint, models of Uranus' moon Titania are relevant since the two objects share similar physical properties (density, size). Castillo-Rogez et al. (2023) found that Titania could preserve a thick (~ 80 km) outer layer that is a porous mixture of ice and rock. Since Haumea's surface is colder than Titania's by 20 to 50 K, one should also expect the dwarf planet to also preserve an undifferentiated outer layer, a case that is consistent with the shell density derived from the shape. Noviello et al. (2022) assumed that Haumea formed from the impact of two large KBOs but did not model the energy involved in the impact and the post-impact internal evolution.

### 4.4. Expectations for the 2026 occultation

As mentioned above, Haumea's equatorial major axis was not visible at the time of the 2017 occultation, making the possible deviation to the ellipsoid invisible. However, at the time of the predicted occultation of May 4, 2026, the rotational phase would be of 0.92, meaning the equatorial major axis could be visible. As a consequence, the projected shape could greatly deviate from an ellipse. Figure 4 shows the predicted shape for configuration C, which corresponds to the case where the deviation between the hydrostatic model and the best-fit ellipsoid of Ortiz et al. (2017) is the most visible, and thus the most likely to be detected by stellar occultation. If Haumea is very close to the critical rotation, we then expect a pinched shape that would be visible at the ends of the equatorial major axis. Otherwise, we expect the shape to be closer to an ellipse and to the shape predicted by the best-fit model of Ortiz et al. (2017) for the 2017 occultation. Thus, the most decisive parts to observe in order to distinguish between the models, and thus conclude on the hydrostaticity of Haumea, are the northern and southern limbs of the shadow. Should the pinched shape be observed with this stellar

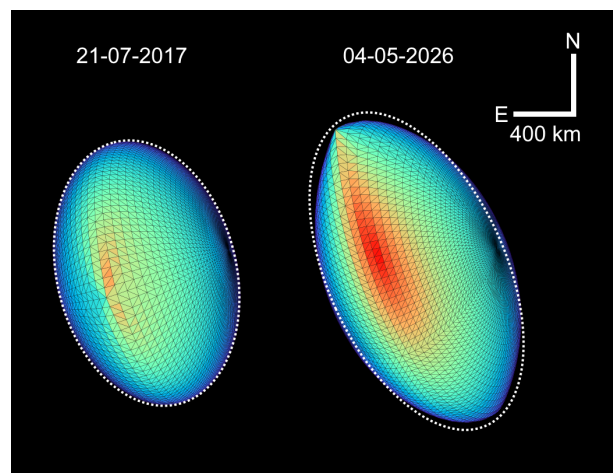


**Fig. 4.** Projections of the hydrostatic shape of configuration C in the sky plane at the time of the 2017 occultation (left) and the future 2026 occultation (right). The projection of the ellipsoidal shape derived by Ortiz et al. (2017) is shown in white dotted line for comparison. The facet colours code the relative irradiance they receive, red being the highest and purple-blue the lowest.

occultation, this would support the assumption that Haumea is close to a hydrostatic body at the critical rotation and thus would support the scenario of the creation of the haumean family by mass shedding proposed by Ortiz et al. (2012) and Noviello et al. (2022).

*Acknowledgements.* We are grateful to B. Sicardy for fruitful discussions about the occultations of 2017 and 2026 and to S. Charnoz for informed comments on the manuscript before submission. This work has been supported by the French Agence Nationale de la Recherche, project Roche, number ANR-23-CE49-0012.

## References

- Barnouin, O., Ballouz, R.-L., Marchi, S., et al. 2024, *Nature Communications*, 15, 6202
- Barr, A. C. & Schwamb, M. E. 2016, *MNRAS*, 460, 1542
- Brozović, M. & Jacobson, R. A. 2024, *AJ*, 167, 256
- Castillo-Rogez, J., Weiss, B., Beddingfield, C., et al. 2023, *Journal of Geophysical Research: Planets*, 128, e2022JE007432
- Chambat, F., Vermersch, J., & Rambaux, N. 2023, *A&A*, 675, L2
- Dunham, E. T., Desch, S. J., & Probst, L. 2019, *ApJ*, 877, 41
- Hamy, M. 1889, *Annales de l'Observatoire de Paris*, 19, F.1
- Holler, B. J., Grundy, W. M., Buie, M. W., & Noll, K. S. 2021, *Icarus*, 355, 114130
- Jorda, L., Lamy, P. L., Gaskell, R. W., et al. 2012, *Icarus*, 221, 1089
- Kondratyev, B. P. 2016, *Ap&SS*, 361, 169
- Kondratyev, B. P. 2024, *Astronomy Reports*, 68, 1449
- Lacerda, P., Jewitt, D., & Peixinho, N. 2008, *AJ*, 135, 1749
- Lanzano, P. 1982, *Deformations of an Elastic Earth* (New York: Academic Press)
- Lockwood, A. C., Brown, M. E., & Stansberry, J. 2014, *Earth Moon and Planets*, 111, 127
- Maeder, A. & Meynet, G. 2012, *Rev. Mod. Phys.*, 84, 25
- McKinnon, W. B., Glein, C. R., Bertrand, T., & Rhoden, A. R. 2020, *arXiv preprint arXiv:2011.14030*
- Murray, C. D. & Dermott, S. F. 1999, *Solar System Dynamics* (Cambridge: Cambridge University Press)
- Noviello, J. L., Desch, S. J., Neveu, M., Proudfoot, B. C. N., & Sonnett, S. 2022, *The Planetary Science Journal*, 3, 225
- Ortiz, J. L., Santos-Sanz, P., Sicardy, B., et al. 2017, *Nature*, 550, 219
- Ortiz, J. L., Thirouin, A., Campo Bagatin, A., et al. 2012, *MNRAS*, 419, 2315
- Proudfoot, B. C. N., Ragozzine, D. A., Giforos, W., et al. 2024, *The Planetary Science Journal*, 5, 69
- Rizos, J. L., Ortiz, J. L., Gutierrez, P. J., Navajas, I. M., & Lara, L. M. 2025, *A&A*, 703, A178
- Staelen, C. & Huré, J.-M. 2026, *A&A*, accepted for publication
- Vermersch, J., Rambaux, N., & Sicardy, B. 2025, *Philos. Trans. A Math. Phys. Eng. Sci.*, 383, 20240186
- Zharkov, V. N. & Trubitsyn, V. P. 1978, *Physics of planetary interiors* (Tucson: Pachart Publishing House)

## Appendix A: Light curves

The Hapke model was used for the reflectance of Haumea, with the same parameters as [Lockwood et al. \(2014\)](#) and a darker spot covering a quarter of Haumea with a 10 % albedo variation ([Lacerda et al. 2008](#)). We reproduce three light curves reported in [Lacerda et al. \(2008\)](#), [Lockwood et al. \(2014\)](#) and [Ortiz et al. \(2017\)](#); the results are shown in figure A.1. Note that only the light curve obtained with configuration C is plotted in figure A.1, but the curves obtained with the other configurations are actually similar to the one reported here. The pinched shape leaves a mark in the light curve, with slightly narrower maxima and slightly larger minima. However, this feature would be difficult to detect on real light curves due to the limited resolution or albedo variations on the surface. Thus, it appears that only stellar occultation could allow us to observe if Haumea has an ellipsoidal or a pinched shape.

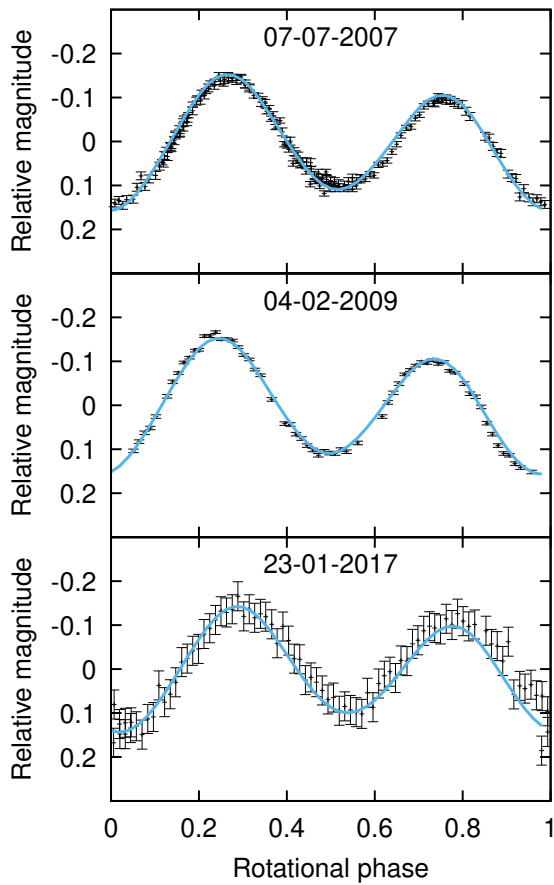


**Fig. A.1.** Comparisons between the light curves of Haumea reported by [Lacerda et al. \(2008, top\)](#), [Lockwood et al. \(2014, middle\)](#) and [Ortiz et al. \(2017, bottom\)](#) and synthetic light curves obtained with the hydrostatic figures.